

# Ex vivo hypercellular parathyroid gland differentiation using dynamic optical contrast imaging (DOCI)

SHAN HUANG,<sup>1,2</sup>  YAZEED ALHIYARI,<sup>1,3,4</sup> YONG HU,<sup>1</sup> KENRIC TAM,<sup>1</sup> ALBERT Y. HAN,<sup>1</sup> JEFFREY F. KRANE,<sup>5</sup> RAMESH SHORI,<sup>6</sup> MAIE A. ST. JOHN,<sup>1,3,4,5</sup> AND OSCAR STAFSUDD<sup>6,\*</sup>

<sup>1</sup>Department of Head and Neck Surgery, University of California Los Angeles, Los Angeles, CA 90095, USA

<sup>2</sup>Department of Materials Science and Engineering, University of California Los Angeles, Los Angeles, CA 90095, USA

<sup>3</sup>UCLA Head and Neck Cancer Program, University of California Los Angeles, Los Angeles, CA 90095, USA

<sup>4</sup>Jonsson Comprehensive Cancer Center, University of California Los Angeles, Los Angeles, CA 90095, USA

<sup>5</sup>Department of Pathology and Laboratory Medicine, University of California Los Angeles, Los Angeles, CA 90095, USA

<sup>6</sup>Department of Electrical and Computer Engineering, University of California Los Angeles, Los Angeles, CA 90095, USA

\*stafsudd@ee.ucla.edu

**Abstract:** Primary hyperparathyroidism, often caused by a single adenoma (80-85%) or four-gland hyperplasia (10-15%), can lead to elevated parathyroid hormone (PTH) levels and resultant hypercalcemia. Surgical excision of offending lesions is the standard of care, as the removal of pathologic adenomas reduces PTH and calcium values to baseline. The small size, variable location, and indistinct external features of parathyroid glands can make their identification quite challenging intraoperatively. Our group has developed the dynamic optical contrast imaging (DOCI) technique, a novel realization of dynamic temporally dependent measurements of tissue autofluorescence. In this study, we evaluated the efficacy of using the DOCI technique and normalized steady-state fluorescence intensity data for differentiating types of human parathyroid and thyroid tissues. We demonstrate that the DOCI technique has the capability to distinguish normal parathyroid tissue from diseased parathyroid glands as well as from adjacent healthy thyroid and adipose tissue across 8 different spectral channels between 405nm-600nm ( $p < 0.05$ ). Patient tissue DOCI data was further analyzed with a logistic regression classifier trained across the 8 spectral channels. After computer training, the computer-aided identification was able to accurately locate hypercellular parathyroid tissue with 100% sensitivity and 98.8% specificity within the captured DOCI image.

© 2022 Optica Publishing Group under the terms of the [Optica Open Access Publishing Agreement](#)

## 1. Introduction

Primary hyperparathyroidism is one of the most common endocrine diseases, with an estimated prevalence of 0.86% in the United States [1]. Primary hyperparathyroidism is often caused by a solitary adenoma (80% - 85%), four-gland hyperplasia (10% - 15%) or carcinoma (<1%) resulting in elevated parathyroid hormone (PTH) [2]. Surgical excision of pathological gland is the standard of care as removal of the affected lesion effectively lowers PTH to normal limits [3]. Parathyroid glands can be difficult to identify intraoperatively as they have variable locations and indistinct visual and palpable features from surrounding fat, thymus, and lymph nodes, making parathyroid gland surgeries challenging. Inadvertent removal or devascularization of normal parathyroid tissue may result in significant morbidity and hypocalcemia [4].

Several preoperative imaging modalities such as ultrasonography, four-dimensional parathyroid computed tomography (4D-CT), magnetic resonance imaging (MRI), and technetium-99m sestamibi scintigraphy are available for parathyroid localization. However, these methods are often insufficient to completely and accurately identify the correct location of the parathyroid glands, and in as many as 10% of operations the affected parathyroid gland is not localized [5,6]. The establishment of intraoperative methods for parathyroid identification would greatly increase the success of gland localization, and thus would potentially help reduce the number of surgical complications [7]. While surgeons conventionally rely on frozen section histologic analysis because it accurately confirms the parathyroid tissue, the approach is invasive, time-consuming and costly [8]. Recently, various novel invasive and non-invasive methods have been developed as intraoperative adjuncts, such as methylene blue (MB) staining [9,10], indocyanine green (ICG) angiography, [11,12] and near-infrared (NIR) autofluorescence (NIRAF) [13,14]. MB stains parathyroid glands after intravenous administration, thus making parathyroid glands visible. ICG marks parathyroid glands via fluorescence when excited with NIR light. However, both MB and ICG may localize non-specifically to thyroid glands [15,16], which can present complications for the accurate identification of the parathyroid glands. In addition, while intravenous administration of ICG and MB are overall well tolerated by the majority of patients, adverse effects can occur ranging from dermatitis to anaphylaxis [17,18]. NIRAF is based on the autofluorescence of parathyroid glands excited by near infrared light. However, the detection of the autofluorescence is negatively impacted by ambient light [19]. The future goal for facile and clinically relevant intraoperative parathyroid identification should be non-invasive, easy to implement and affordable.

Our group developed dynamic optical contrast imaging (DOCI), a novel imaging modality that can probe the composition variations of a sample by measuring the aggregate fluorescence decay activity. A variety of endogenous fluorophores exist in human tissues which enable the non-invasive determination of tissue composition via the use of the DOCI technique. Previously, we have shown that DOCI can be used for fast and wide-field identification of the parathyroid gland [20,21]. Since primary hyperparathyroidism is most often caused by solitary adenomas [2], it would be highly beneficial to be able to distinguish between hypercellular parathyroid adenomas and normal parathyroid glands. In this study, we demonstrate that DOCI and integrated machine learning algorithms can be utilized to visually differentiate and classify hypercellular parathyroid adenomas from normal parathyroid glands and surrounding tissue.

## **2. Materials and methods**

### *2.1. Tissue collection*

The acquisition of human tissue specimens for this study was approved by the University of California, Los Angeles (UCLA) Institutional Review Board. Suitable human subjects were identified from patients who underwent parathyroid and thyroid surgery at Ronald Reagan UCLA Medical Center. The tissue specimens were imaged with DOCI immediately post resection. For each specimen imaged via DOCI, the tissue type composition of a corresponding sample was confirmed using H&E histology by a blinded head and neck pathologist (JFK). A total of 115 tissue specimen were obtained from 47 patients.

### *2.2. DOCI instrumentation*

An ex vivo DOCI setup was used for imaging and the system details have been described previously [22]. The DOCI setup is shown in Fig. 1(A). Briefly, the system consists of an imaging unit and an illumination unit. The imaging unit contains an imaging lens (EF 50mm f/1.2L USM, Canon), a motorized filter wheel (X-FWR-E, Zaber) that holds 8 optical filters inside and an intensified charge-coupled device (iCCD) (iStar DH334T-18U-A3, Andor). The illumination unit contains a custom-developed ultraviolet light-emitting diode (UV-LED) circuit board, a liquid

light guide (LLG5-4T, Thorlabs) and a collimator lens (ACL25416U-A, Thorlabs). The single UV-LED light source has a center wavelength at 365 nm and a full width at half max (FWHM) of 14 nm. With a repetition rate of 500 kHz and a pulse width of 80 ns, the pulsed light delivers a 4 W/m<sup>2</sup> power onto the sample. This power complies with NIOSH UV radiation exposure limits [23]. The fluorescence emission is spectrally resolved into 8 spectral channels using one 405 nm long-pass filter (LPF) (BLP01-405R-25, Semrock) to ensure blockage of all excitation source light, and 7 band-pass filters (BPF) with center wavelength/FWHM of: 434/17 nm (FF01-434/17-25, Semrock), 465/30 nm (FF01-465/30-25, Semrock), 494/20 nm (FF01-494/20-25, Semrock), 520/15 nm (FF01-520/15-25, Semrock), 542/27 nm (FF01-542/27-25, Semrock), 572/28 nm (FF01-572/28-25, Semrock), and 605/15 nm (FF01-605/15-25, Semrock). Figure 1(B) shows the image acquisition process wherein 3 images are acquired from 3 different phases of the emission pulse: steady-state ( $I_{SS}$ ), decay-state ( $I_{DS}$ ) and background ( $I_{BG}$ ).

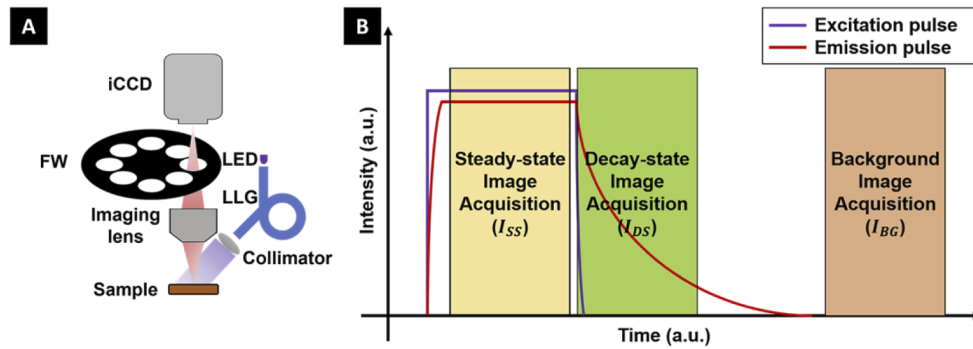


**Fig. 1.** (A) Schematic presentation of the imaging apparatus, modified from [21]. (B) Diagram of the image acquisition process. iCCD: intensified charge-coupled device. FW: filter wheel. LED: light-emitting diode. LLG: liquid light guide.

### 2.3. Image processing

A DOCI image was computed for all 8 filter channels, and a normalized intensity image was computed for all 7 BPF channels. An aggregate intensity measurement was recorded from the moment the illumination started to decrease until the fluorescence ceased. The DOCI image ( $I_{DOCI}$ ) was calculated by normalizing the aggregate fluorescence decay intensity ( $I_{DS}$ ) to the aggregate steady-state fluorescence intensity ( $I_{SS}$ ) [21]:

$$I_{DOCI} = \frac{I_{DS} - I_{BG}}{I_{SS} - I_{BG}} \quad (1)$$

For each BPF channel, the normalized intensity image ( $I_{norm,BPF}$ ) was calculated from the ratio of the aggregate steady-state fluorescence intensities between the BPF channel ( $I_{SS,BPF}$ ) and the 405 nm LPF channel ( $I_{SS,LPF}$ ):

$$I_{norm,BPF} = \frac{I_{SS,BPF}}{I_{SS,LPF}} \quad (2)$$

Normalization was applied to the steady-state fluorescence intensity data to alleviate the intensity variance caused by uneven illumination and rugged specimen surface.

### 2.4. Statistical analysis and machine learning classification

The data analyses were performed with MATLAB R2021a. For each tissue sample with identified tissue type, one region-of-interest (ROI) was selected. For each ROI, the medians of

the multi-spectral DOCI values and normalized intensity values were extracted as features for subsequent analysis. The nonparametric Wilcoxon Rank Sum Test [24] was used to compare the single-channel data between different tissue types. To investigate the classification task of hypercellular parathyroid versus other types of tissue, we selected 3 classifier models that have been adapted to multivariate analysis and classification of topics with complex samples in the biomedical community: logistic regression (LR) [25,26], k-nearest neighbors (KNN) [27,28] and artificial neural networks (ANN) [29]. The leave-one-out cross-validation was applied for classification performance evaluation: for each fold, one specimen was tested on the classifier model trained with the remaining specimens, this was repeated for all specimens and the mean performance was calculated.

### 3. Results

Of the 47 patients included in this study, 29 patients had at least one parathyroid gland removed, 23 patients had thyroid tissue removed, and 4 patients had both parathyroid and thyroid tissue removed (all based on clinical indications). Table 1 outlines all tissue specimens collected from the 47 individuals.

**Table 1. Tissue Specimens Imaged Using DOCI**

Tissue type	Count	Specimens	Patients
Hypercellular parathyroid	31	32.3%	55.3%
Normal parathyroid	6	6.3%	8.5%
Thyroid	35	36.5%	48.9%
Thymus	7	7.3%	12.8%
Lymph node	13	13.5%	14.9%
Adipose	23	24.0%	31.9%

Figure 2 demonstrates the DOCI results of different tissues collected from the same patient. The 405 nm LPF channel DOCI scans of three specimens are displayed here: hypercellular parathyroid (Fig. 2(A)), thyroid (Fig. 2(B)) and adipose (Fig. 2(C)). Corresponding H&E histology images

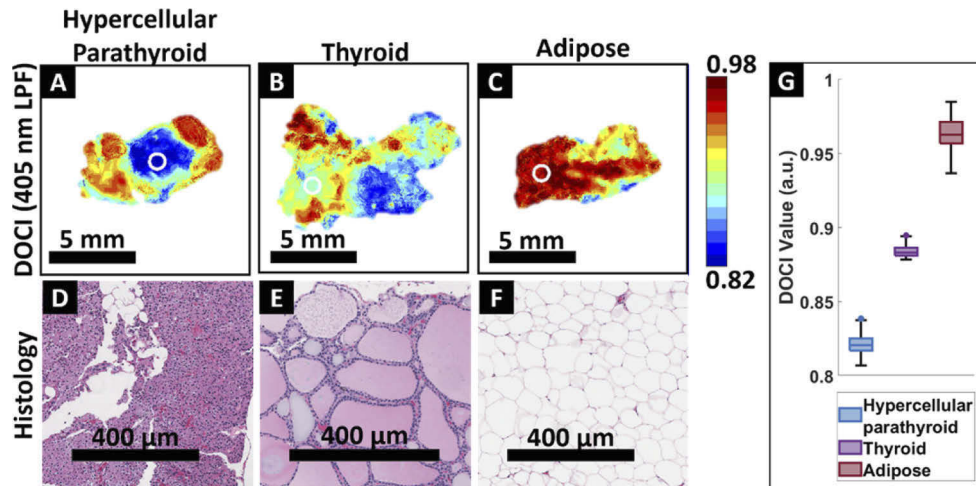


**Fig. 2.** DOCI images of parathyroid (A), thyroid (B) and adipose (C) tissues, which were collected from the same patient. (D) - (F) Corresponding H&E histology confirms tissue composition. (G) Box plot of DOCI data from white circular ROIs marked on (A) - (C)

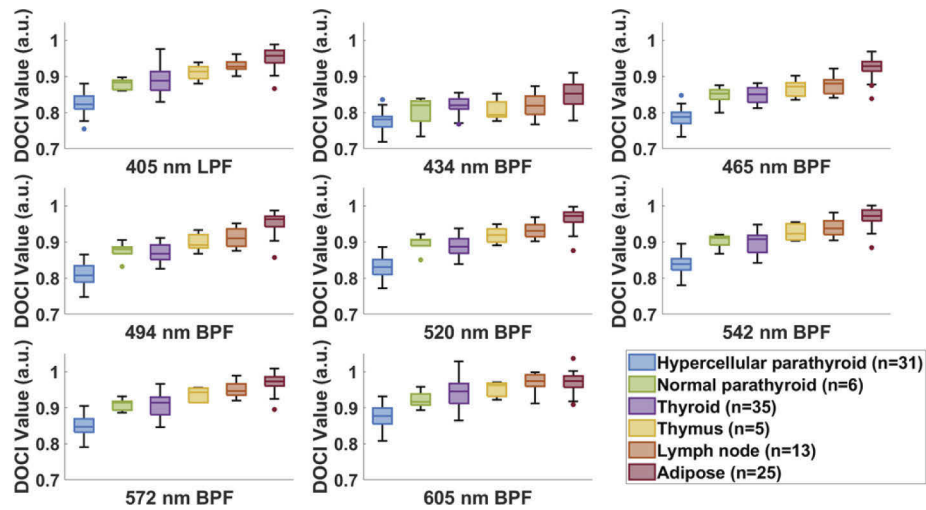


**Fig. 3.** Box plots of DOCI value medians for all tissue types.

(Fig. 2(D-F)) are shown below each DOCI image. Circular ROIs are highlighted in the DOCI images. The labeled tissue type only applies to the tissues in the ROI. The histology is matching the specific ROI portion. DOCI data from selected ROIs (Fig. 2(G)) show that the DOCI value of hypercellular parathyroid is smaller than thyroid ( $p < 0.001$ ) and adipose ( $p < 0.001$ ).

For each ROI, a total of 15 features were extracted: DOCI values from all 8 filter channels and normalized intensity values from 7 BPF channels. These features were grouped by tissue type and tested for statistical significance. Figure 3 shows the grouped box plot of DOCI values for each filter channel, and Fig. 4 shows the grouped box plot of normalized intensity value for each BPF channel. The Wilcoxon Rank Sum Test was used for comparing hypercellular parathyroid with other tissue types, Fig. 5 and Fig. 6 show the Manhattan plots of calculated P

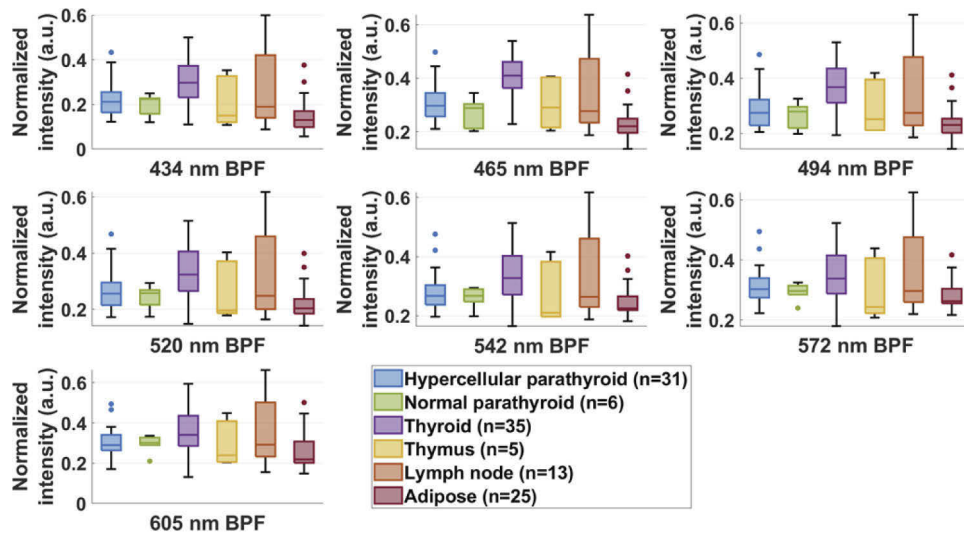


**Fig. 4.** Box plots of normalized steady-state fluorescence intensity value medians for all tissue types.



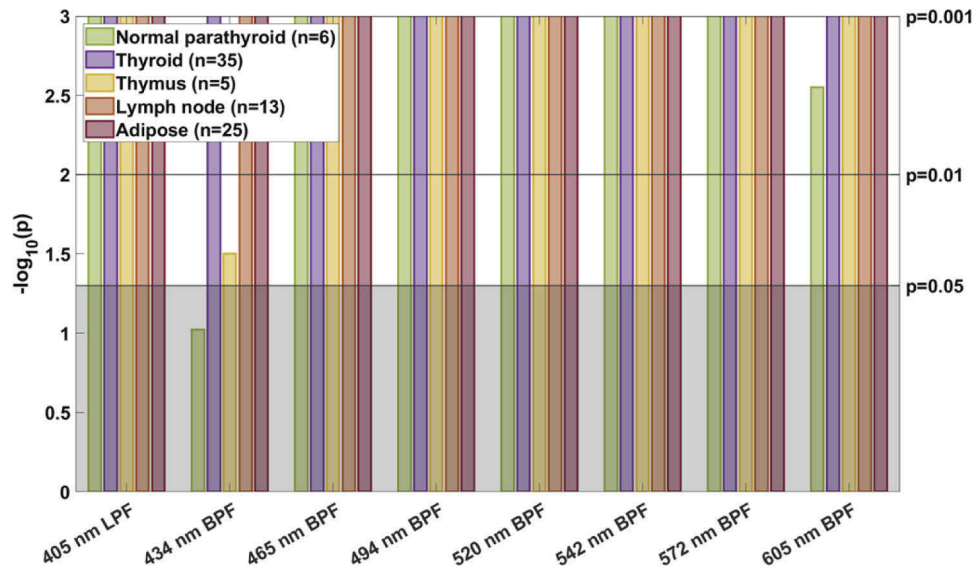


**Fig. 5.** P values of DOCI value displayed as Manhattan plots, P values were calculated from the Wilcoxon Rank Sum Test between hypercellular parathyroid and other 5 tissue types.  $p < 0.05$  is labeled as significant,  $p = 0.01$  and  $p = 0.001$  are also marked for reference.

values. A significant difference ( $p < 0.05$ ) in DOCI value was observed between hypercellular parathyroid and other tissue types for all 8 filter channels, except for hypercellular parathyroid versus normal parathyroid in the 434 nm BPF channel. Additionally, a significant difference ( $p < 0.05$ ) in normalized intensity value was observed between hypercellular parathyroid and two types of tissue, thyroid and adipose, for all 7 BPF channels.

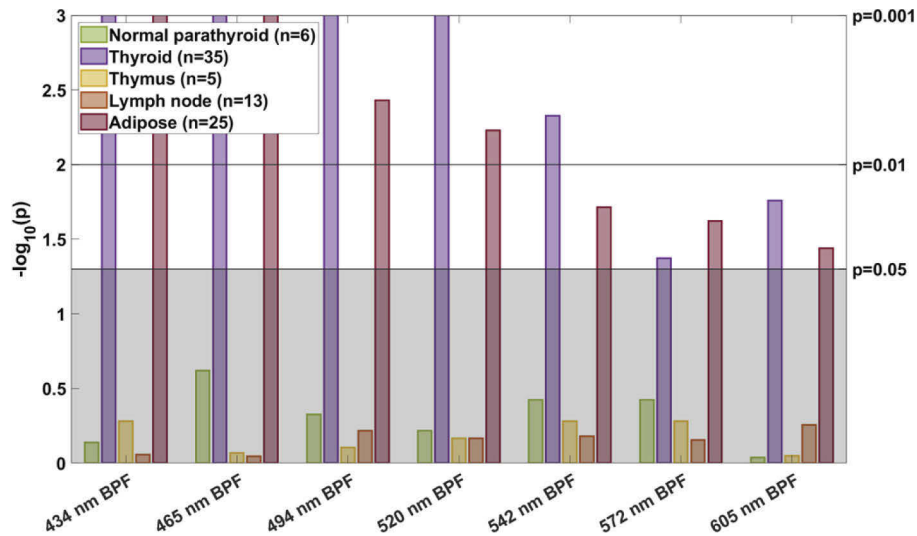


**Fig. 6.** P values of normalized steady-state fluorescence intensity value displayed as Manhattan plots, P values were calculated from the Wilcoxon Rank Sum Test between hypercellular parathyroid and other 5 tissue types.  $p < 0.05$  is labeled as significant,  $p = 0.01$  and  $p = 0.001$  are also marked for reference.

The classification of hypercellular parathyroid was evaluated on 3 data sets with a different number of features: DOCI value from the 405 LPF channel; DOCI values from all 8 filter channels; DOCI values from all 8 filter channels and normalized intensity values from all 7 BPF channels. Three classifier models were evaluated: LR, KNN ( $k=11$ ) and ANN (activation function: ReLU). Table 2 presents the classification results on the 3 data sets, the sensitivity and specificity of each classifier model are displayed in the table. With more features included as the input, the classification performance improved and eventually reached 100% sensitivity and 98.8% specificity with the logistic regression classifier. Figure 7 shows the receiver operating characteristic (ROC) curves for comparisons between different classifier models on different data sets.

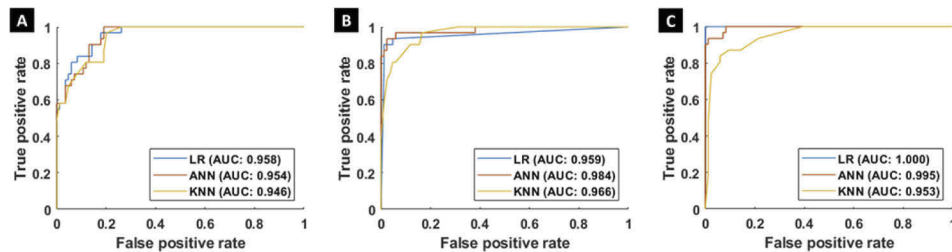


**Fig. 7.** ROC curves for the 3 classifier models on: (A) 405 nm LPF channel DOCI value data set; (B) All 8 filter channels DOCI value data set; (C) All 8 filter channels DOCI value & all 7 BPF channels normalized intensity value data set. AUC: area under the curve.

**Table 2. Classification Performance of 3 Classifier Models on 3 Data Sets<sup>a</sup>**

Features (n) <sup>a</sup>	Model		
	LR	KNN	ANN
405 nm LPF channel DOCI (1)	80.6% / 94.0%	74.2% / 91.7%	67.7% / 95.2%
All 8 filter channels DOCI (8)	90.3% / 95.2%	80.6% / 94.0%	87.1% / 96.4%
All 8 filter channels DOCI & all 7 BPF channels normalized intensity (15)	100% / 98.8%	83.9% / 94.0%	93.5% / 96.4%

<sup>a</sup>The two percentages in each cell are sensitivity and specificity, respectively.

<sup>b</sup>n: number of features.

#### 4. Discussion

The variable location and indistinct external features of parathyroid glands can make their intraoperative identification challenging during parathyroidectomies. While inadequate removal of a diseased gland results in a prolonged surgery or reoperation, inadvertent removal of normal parathyroid glands results in clinical hypocalcemia [21]. The results presented in this study demonstrate that DOCI can be used as an adjunct diagnostic method to effectively distinguish hypercellular parathyroid glands from normal parathyroid glands and adjacent tissues, including, thyroid, thymus, and lymph nodes. Previous publications have identified biologically relevant endogenous fluorophores that produce the lifetime contrast differences in tissues. The most notable fluorophores include nicotinamide adenine dinucleotide (NADH), flavin adenine dinucleotide (FAD), elastin, and collagen [30]. The DOCI system principally characterizes lifetime by computing the ratio between the aggregate fluorescence decay intensity and the

aggregate fluorescence steady-state intensity, thus allowing us to discriminate tissues based on their unique composition.

Across 8 different spectral channels, hypercellular parathyroid tissue was shown to have lower DOCI values when compared with normal parathyroid, thyroid, thymus, lymph node and adipose tissue. The observed relationship of DOCI value between parathyroid tissue and other tissue types is concordant with previous publications and reported fluorescence lifetime data [31,32]. Throughout all spectrally gated channels, there is an increasing trend among the DOCI values of hypercellular parathyroid, normal parathyroid and adipose tissue. Histologically, normal parathyroid gland is composed mainly of chief cells and adipocytes with thin fibrous septa dividing the gland into lobules, while hypercellular parathyroid is usually characterized by chief cell proliferation and absent or reduced stromal adipocytes [33]. It is likely the DOCI value difference between hypercellular parathyroid, normal parathyroid and adipose tissue may be related to the change in the ratio between chief cells and adipocytes. Furthermore, the increased metabolic demand in the development of hypercellular parathyroid vs normal would potentially favor free NADH (lifetime 0.4ns) versus parathyroid with oxidative phosphorylation or bound NADH (lifetime 1 to 5ns), whereas fat stores retinol, a fluorescent compound with a 12ns lifetime when bound [34]. This pattern of hypercellular parathyroid, normal parathyroid and fat having the shortest, intermediate, and longest lifetime respectively is also supported within our DOCI data (Fig. 3).

Since the DOCI calculation is formulated from the intensity image captured at steady state, decay state and background, the fluorescence intensity information can also be used as an input feature of the classifier to discriminate tissues or potentially fluorophores. Our previous works [20,21,35,36] solely investigated the DOCI values. However here we demonstrate that adding the steady state fluorescent information with DOCI values provided a more robust AI training module. For the 2-class classification of hypercellular parathyroid against other tissue types, we observed pronounced improvement in classification performance after normalized steady-state fluorescence intensity was added as input for all three classifier models (Table 2). Specifically, the highest sensitivity (100%) and specificity (98.8%) were from the logistic regression classifier trained on the comprehensive features from combined DOCI and normalized steady-state fluorescence intensity data, the addition of fluorescence intensity information helped increase 9.7% and 3.6% in sensitivity and specificity, respectively. The LR classifier model was the best fitting model, it suggests that the predicted probability of tissue type is a linear combination of multi-channel DOCI value and fluorescence intensity features. Benefited from the unique working principle of DOCI [21], the acquisition of fluorescence emission profile is an indispensable step. In other words, from the perspective of data acquisition, there is zero extra cost to add the steady-state fluorescence intensity data to data analysis. Data processing will add additional calculations, but because the overall data processing calculations are already very light, the additional calculation costs are affordable or even negligible.

DOCI imaging is rapid; it takes less than 2 seconds to acquire DOCI contrast across a wide field image. DOCI utilizes a non-ionizing light source and builds contrast based on a sample's autofluorescence. It allows for rapid and non-invasive probing of tissue composition, which makes it a reliable intraoperative adjunct imaging technique to find the location of hypercellular parathyroid glands. This study provided us with the feasibility that the DOCI technique can be used for hypercellular parathyroid localization.

Patient prognosis depends heavily on complete resection of the involved parathyroid glands. DOCI is a compact, user friendly, non-invasive, clinically relevant imaging system that can precisely detect parathyroid tissue and differentiate normal from hypercellular diseased glands. The DOCI system is clinically relevant and easily operable by clinical providers to better inform and improve the treatment of patients undergoing thyroid, parathyroid and neck surgery.



## 5. Conclusion

Advances in intraoperative parathyroid localization and diagnostics continue to be a major need in our treatment of patients with thyroid and parathyroid disease. The small size, variable location, and indistinct external features of parathyroid glands can make their identification quite challenging intraoperatively. Patient prognosis depends heavily on complete resection of the involved parathyroid glands. There remains a large gap in this area and improvement of intraoperative detection will be a key to optimize treatment and patient outcomes.

In this study, we demonstrated that DOCI can discriminate between a variety of tissues and with the incorporation of AI techniques, allows DOCI to specifically identify hypercellular parathyroid with greater confidence. We show statistically significant differences in DOCI values and normalized steady-state intensity values between hypercellular parathyroid glands, normal parathyroid glands and adjacent tissues. We observed a best performance of 100% sensitivity and 98.8% specificity on classification of hypercellular parathyroid. This work lays the foundation for future in vivo research using DOCI as the basis of intraoperative instruments to guide the localization of parathyroid glands, and then to determine if they are normal or hypercellular. In the future, DOCI can serve as a platform for the early detection of specific tissue types throughout the body.

**Funding.** National Institutes of Health (R01CA205051, RD1DE026654).

**Acknowledgments.** The authors thank the Translational Pathology Core Laboratory (TPCL) at UCLA and Surgical Pathology at UCLA for infrastructure and support.

**Disclosures.** The authors declare no conflicts of interest.

**Data availability.** Data underlying the results presented in this paper are not publicly available at this time but may be obtained from the authors upon reasonable request.

## References

1. D. M. Press, A. E. Siperstein, E. Berber, J. J. Shin, R. Metzger, J. Jin, R. Monteiro, J. Mino, W. Swagel, and J. C. Mitchell, "The prevalence of undiagnosed and unrecognized primary hyperparathyroidism: a population-based analysis from the electronic medical record," *Surgery* **154**(6), 1232–1238 (2013).
2. R. A. DeLellis, P. Mazzaglia, and S. Mangray, "Primary hyperparathyroidism: a current perspective," *Arch. Pathol. Lab. Med.* **132**(8), 1251–1262 (2008).
3. B. C. Silva, N. E. Cusano, and J. P. Bilezikian, "Primary hyperparathyroidism," *Best Pract. Res. Clin. Endocrinol. Metab.* **32**(5), 593–607 (2018).
4. J. Baj, R. Sitarz, M. Lokaj, A. Forma, M. Czezelewski, A. Maani, and G. Garruti, "Preoperative and intraoperative methods of parathyroid gland localization and the diagnosis of parathyroid adenomas," *Molecules* **25**(7), 1724 (2020).
5. A. Mohebbati and A. R. Shaha, "Imaging techniques in parathyroid surgery for primary hyperparathyroidism," *Am. J. Otolaryngol.* **33**(4), 457–468 (2012).
6. A. Wong, J. C. Wong, P. U. Pandey, and S. M. Wiseman, "Novel techniques for intraoperative parathyroid gland identification: a comprehensive review," *Expert Rev. Endocrinol. Metab.* **15**(6), 439–457 (2020).
7. M. Schneider, V. Dahm, C. Passler, E. Sterrer, G. Mancusi, R. Repasi, E. Gschwandtner, E. Fertl, L. Handgriff, and M. Hermann, "Complete and incomplete recurrent laryngeal nerve injury after thyroid and parathyroid surgery: Characterizing paralysis and paresis," *Surgery* **166**(3), 369–374 (2019).
8. A. K. Dewan, S. B. Kapadia, C. S. Hollenbeak, and B. C. Stack Jr, "Is routine frozen section necessary for parathyroid surgery?" *Otolaryngol.–Head Neck Surg.* **133**(6), 857–862 (2005).
9. N. E. Dudley, "Methylene blue for rapid identification of the parathyroids," *Br. Med. J.* **3**(5776), 680–681 (1971).
10. J. Bewick and A. Pfeleiderer, "The value and role of low dose methylene blue in the surgical management of hyperparathyroidism," *Ann. R. Coll. Surg. Engl.* **96**(7), 526–529 (2014).
11. P. Jitpratoom and A. Anuwong, "The use of ICG enhanced fluorescence for the evaluation of parathyroid gland preservation," *Gland Surg.* **6**(5), 579–586 (2017).
12. S. M. Sadowski, J. V. Fortuny, and F. Triponez, "A reappraisal of vascular anatomy of the parathyroid gland based on fluorescence techniques," *Gland Surg.* **6**(S1), S30–S37 (2017).
13. C. Paras, M. Keller, A. Mahadevan-Jansen, L. White, and J. Phay, "Near-infrared autofluorescence for the detection of parathyroid glands," *J. Biomed. Opt.* **16**(6), 067012 (2011).
14. M. A. McWade, C. Paras, L. M. White, J. E. Phay, C. C. Solórzano, J. T. Broome, and A. Mahadevan-Jansen, "Label-free intraoperative parathyroid localization with near-infrared autofluorescence imaging," *J. Clin. Endocrinol. Metab.* **99**(12), 4574–4580 (2014).

15. S. W. Kim, S. H. Song, H. S. Lee, W. J. Noh, C. Oak, Y.-C. Ahn, and K. D. Lee, "Intraoperative real-time localization of normal parathyroid glands with autofluorescence imaging," *J. Clin. Endocrinol. Metab.* **101**(12), 4646–4652 (2016).
16. R. M. Devine, J. A. Van Heerden, C. S. Grant, and J. J. Muir, "The role of methylene blue infusion in the management of persistent or recurrent hyperparathyroidism," *Surgery* **94**(6), 916–918 (1983).
17. W. Chu, A. Chennamsetty, R. Toroussian, and C. Lau, "Anaphylactic shock after intravenous administration of indocyanine green during robotic partial nephrectomy," *Urol. Case Rep.* **12**, 37–38 (2017).
18. P. Dewachter, C. Mouton-Faivre, P. Trechot, J.-C. Lleu, and P. M. Mertes, "Severe anaphylactic shock with methylene blue instillation," *Anesth. Analg.* **101**(1), 149–150 (2005).
19. B. Kahramangil, F. Dip, F. Benmiloud, J. Falco, M. de La Fuente, S. Verna, R. Rosenthal, and E. Berber, "Detection of parathyroid autofluorescence using near-infrared imaging: a multicenter analysis of concordance between different surgeons," *Ann. Surg. Oncol.* **25**(4), 957–962 (2018).
20. I. A. Kim, Z. D. Taylor, H. Cheng, C. Sebastian, A. Maccabi, J. Garritano, B. Tajudeen, A. Razfar, F. Palma Diaz, and M. Yeh, "Dynamic optical contrast imaging: A technique to differentiate parathyroid tissue from surrounding tissues," *Otolaryngol.–Head Neck Surg.* **156**(3), 480–483 (2017).
21. Y. Hu, A. Y. Han, S. Huang, P. Pellionisz, Y. Alhiyari, J. F. Krane, R. Shori, O. Stafsudd, and M. A. St. John, "A tool to locate parathyroid glands using dynamic optical contrast imaging," *Laryngoscope* **131**(10), 2391–2397 (2021).
22. Y. Hu, A. S. Moon, P. Pellionisz, S. Huang, O. Stafsudd, and M. S. John, "Design and validation of an intraoperative autofluorescence lifetime imaging device," *Proc. SPIE* **11213**, 1121309 (2020).
23. N. I. f. O. Safety and Health, *Criteria for a Recommended Standard: Occupational Exposure to Ultraviolet Radiation* (1972).
24. M. Hollander, D. A. Wolfe, and E. Chicken, *Nonparametric statistical methods* (John Wiley & Sons, 2013), Vol. 751.
25. A. J. Walsh, K. P. Mueller, K. Tweed, I. Jones, C. M. Walsh, N. J. Piscopo, N. M. Niemi, D. J. Pagliarini, K. Saha, and M. C. Skala, "Classification of T-cell activation via autofluorescence lifetime imaging," *Nat. Biomed. Eng.* **5**(1), 77–88 (2021).
26. K. Samimi, E. C. Guzman, S. M. Trier, D. L. Pham, T. Qian, and M. C. Skala, "Time-domain single photon-excited autofluorescence lifetime for label-free detection of T cell activation," *Opt. Lett.* **46**(9), 2168–2171 (2021).
27. C. A. Gómez, J. Sutin, W. Wu, B. Fu, H. Uhlirova, A. Devor, D. A. Boas, S. Sakadžić, and M. A. Yaseen, "Phasor analysis of NADH FLIM identifies pharmacological disruptions to mitochondrial metabolic processes in the rodent cerebral cortex," *PLoS One* **13**(3), e0194578 (2018).
28. Q. Yang, M. Qi, Z. Wu, L. Liu, P. Gao, and J. Qu, "Classification of skin cancer based on fluorescence lifetime imaging and machine learning," in *Optics in Health Care and Biomedical Optics X*, (International Society for Optics and Photonics, 2020), 115531Y.
29. M. A. K. Sagar, K. P. Cheng, J. N. Ouellette, J. C. Williams, J. J. Watters, and K. W. Eliceiri, "Machine learning methods for fluorescence lifetime imaging (FLIM) based label-free detection of microglia," *Front. Neurosci.* **14**, 931 (2020).
30. M. Y. Berezin and S. Achilefu, "Fluorescence lifetime measurements and biological imaging," *Chem. Rev.* **110**(5), 2641–2684 (2010).
31. M. P. Brandao, R. Iwakura, A. A. Honorato-Sobrinho, K. Haleplian, A. S. Ito, L. C. C. de Freitas, and L. Bachmann, "Optical Characterization of Parathyroid Tissues," *Appl. Spectrosc.* **70**(10), 1709–1716 (2016).
32. M. Marsden, S. S. Weaver, L. Marcu, and M. J. Campbell, "Intraoperative mapping of parathyroid glands using fluorescence lifetime imaging," *J. Surg. Res.* **265**, 42–48 (2021).
33. J. Guilmette and P. M. Sadow, "Parathyroid pathology," *Surg. Pathol. Clin.* **12**(4), 1007–1019 (2019).
34. R. Datta, T. M. Heaster, J. T. Sharick, A. A. Gillette, and M. C. Skala, "Fluorescence lifetime imaging microscopy: fundamentals and advances in instrumentation, analysis, and applications," *J. Biomed. Opt.* **25**(07), 1 (2020).
35. B. A. Tajudeen, Z. D. Taylor, J. Garritano, H. Cheng, A. Pearigen, A. J. Sherman, F. Palma-Diaz, P. Mishra, S. Bhargava, and J. Pesce, "Dynamic optical contrast imaging as a novel modality for rapidly distinguishing head and neck squamous cell carcinoma from surrounding normal tissue," *Cancer* **123**(5), 879–886 (2017).
36. A. J. Sherman, A. Papour, S. Bhargava, M. A. S. John, W. H. Yong, Z. Taylor, W. S. Grundfest, and O. M. Stafsudd, "Normalized fluorescence lifetime imaging for tumor identification and margin delineation," in *Advanced Biomedical and Clinical Diagnostic Systems XI*, (International Society for Optics and Photonics, 2013), 85721H.